

Exploration of the Free Rolling Motion of a Delta Wing Configuration in Vortical Flow

M.T. Arthur¹

QinetiQ, Farnborough, UK

M. Allan²

CFD Group, Department of Aerospace Engineering, University of Glasgow, UK

N. Ceresola³

Alenia Aeronautica, Torino, Italy

J. Kompenhans⁴

DLR, Göttingen, Germany

W. Fritz⁵

EADS(M), Ottobrunn, Germany

and

O.J. Boelens and B.B. Prananta⁶

NLR, Amsterdam, The Netherlands

ABSTRACT

The paper describes the results of a combined computational and experimental study of the free rolling motion of a delta wing fuselage configuration in viscous, vortical flow. The key features of the study are: validation against data obtained in carefully executed experiments; extensive code-to-code comparisons; a spatial grid refinement study using grids with up to 12 million cells; a temporal grid refinement study; an assessment of the impact of different turbulence models on the predicted vehicle motion; and a comparison of two different schemes for implementing a mathematical model of the mechanical friction in the wind-tunnel model support rig. Results showing initial pressure distributions and the histories of the motions, forces and moments are shown for three test cases exhibiting different characteristic motions. Figures illustrating several other features of the study are also presented.

1.0 INTRODUCTION

The paper describes the results of a study of the free rolling motion of a delta wing fuselage configuration in viscous, vortical flow. It is a continuation of the study of the flow over the configuration in forced rolling motion that has been undertaken during recent years within the Western European Armaments Group collaborative programme known as THALES Joint Programme 12.15 [1,2]. The programme has been concerned with the development and validation of computational methods for the prediction of steady and unsteady vortical flows over military aircraft configurations. The stage of development and the

¹ mtarthur@qinetiq.com

² Mark.Allan@ansys.com. Now at ANSYS Europe, Harwell, UK.

³ nceresola@aeronautica.alenia.it

⁴ Juergen.Kompenhans@dlr.de

⁵ willy.fritz@m.eads.net

⁶ boelens@nlr.nl, prant@nlr.nl

computing power now readily available are such that the methods can be exploited in ways beyond the conventional analysis of flows over specified configurations. One such avenue of exploitation is the simulation of free or controlled manoeuvre. To perform such simulations, the equations governing the fluid flow must be augmented with an equation of motion for the vehicle and the complete system must be solved in a time-accurate fashion. This is the subject of the present paper. While it is unrealistic to suggest that the capability could be used for the population of traditional, derivative-based flight mechanics models, it should at the same time be remembered that such models are based on assumptions of linear responses to small perturbations from trimmed states. Their use is therefore inappropriate at the margins of the flight envelope affected by pitch-up, wing drop, nose slice, buffet or wing rock even when higher order stability derivatives are incorporated. In contrast, methods of the type applied here model the non-linear aerodynamics directly and so enable the non-linear behaviour of an air vehicle manoeuvring at high angular rates to be simulated. They can be used to explore limited regions of the flight envelope in both analysis and assessment contexts. Their greatest value will lie in their application early in the design process to reduce risks and avoid the high costs associated with eliminating or avoiding problems later in the development or deployment phases. Computational methods allow exploration of manoeuvres that are difficult to perform in a wind tunnel or dangerous to perform in flight; they can aid the assessment of real vehicles and their control laws and hence also the design of flight simulators.

In the investigation described here, three cases were defined, having different sets of initial and/or boundary conditions which led to vehicle motions with significantly different characteristics. While similar computational capabilities have been developed elsewhere, and results for more complex vehicle motions have been reported, the importance of this study lies in the depth of the investigation and the care with which it was undertaken. The close co-operation between the partners contributing the experimental and computational results significantly enhanced the value of the overall programme. It ensured that appropriate experimental data were obtained, suitable mathematical models could be developed and that the computed results could be validated against experiment. No partner could have undertaken such an extensive investigation on his own. The key features of the present study are, in addition to this close co-operation: the three different types of motion investigated; validation against data obtained in carefully executed experiments; extensive code-to-code comparisons; a spatial grid refinement study using grids with up to 12 million cells; a temporal grid refinement study; an assessment of the impact of different turbulence models on the predicted vehicle motion; and a comparison of two different schemes for implementing a mathematical model of the mechanical friction in the wind-tunnel model support rig. The participants in the programme were Alenia (Italy), EADS-M (Germany), NLR (The Netherlands) and The University of Glasgow and QinetiQ (United Kingdom) for the computational work, and DLR (Germany) for the experimental investigation. Each nation contributed results of calculations for the cases described. The paper includes a description of the test cases, a brief description of the computational methods used by the participants and an outline description of the experiments. The way in which the mathematical model of the mechanical friction in the wind-tunnel support rig was derived is described briefly and the model is defined. A selection of results illustrating the different types of vehicle motion is then presented, including figures showing the difference between wind-tunnel and free-flight behaviour. In addition, some results illustrating other aspects of the study referred to above are presented.

2.0 DESCRIPTION AND DEFINITION OF TEST CASES

The configuration consisted of a cropped delta wing with a sharp leading edge of 65° sweep mounted symmetrically on a fuselage which was for the most part cylindrical but blended smoothly into the wing surface at the junctions. The radius of the cylinder was constant along most of its length but fell smoothly to zero as the apex was approached so that no part of the fuselage lay ahead of the wing leading edge. The wing planform definition is shown in Figure 1 while the model geometry is shown in Figure 2. In each of the cases studied, the configuration was held at incidence in transonic flow at a non-zero roll angle and then released. The subsequent motion was predicted and observed in a wind tunnel. In one of the cases

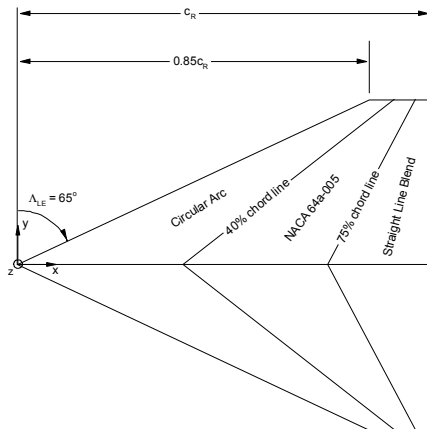


Figure 1: Wing planform definition

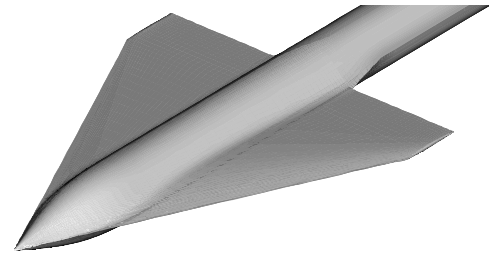


Figure 2: Model geometry

vortex breakdown was not present whereas in the other two breakdown occurred and had a significant impact on the subsequent motion.

The first test case was chosen to help verify that the flight mechanics model, moving mesh treatments and boundary conditions had been implemented correctly in each of the methods. The mechanical friction in the rotating model support system was therefore not included in the computations. When the vehicle was released at roll angle $\phi = \phi_0$, it accelerated towards the symmetric position, $\phi = 0$, then decelerated as it continued in a damped, oscillatory motion about $\phi = 0$.

Mechanical friction was included in the computations of cases 2 and 3 to facilitate meaningful comparisons between experimental and predicted roll histories. Case 2 was particularly interesting because the predicted vehicle motion was very sensitive to the computed rolling moment. In the experiment, the damping was such that the direction of vehicle rotation reversed before the symmetric position $\phi = 0$ was reached. The vehicle then came to rest without overshoot at a non-zero roll angle $\phi = \phi_1 > 0$.

The boundary conditions for case 3 were the same as those for case 2 but the initial roll angle was larger. After release, the angular momentum attained by the vehicle carried it past the final trim position of case 2 and past the symmetric trim position, $\phi = 0$. The vehicle came to rest momentarily before rolling back towards $\phi = 0$. However, with only a slight overshoot, the vehicle motion was halted at a third trim position, $\phi = -\phi_1$. An additional calculation performed by one partner for the same conditions but with no mechanical friction included showed that such singular behaviour was not merely a feature of wind-tunnel models with mechanical friction in their support rigs. It showed a greater initial amplitude of oscillation, as expected, so that the angular momentum of the vehicle carried it past the trim points at $\phi = -\phi_1$ and $\phi = 0$. The vehicle then executed damped sinusoidal oscillations about the final trim position of case 2, $\phi = \phi_1$. Thus singular behaviour may be a feature of both wind-tunnel and free flight experiments.

The boundary and initial conditions for the three cases were:

1. $M_\infty = 0.85$, $\alpha = 9^\circ$, $Re_{\text{cref}} = 4.9 \cdot 10^6$ and $\phi_0 = 40^\circ$ (port wing down);
2. $M_\infty = 0.85$, $\alpha = 17^\circ$, $Re_{\text{cref}} = 4.9 \cdot 10^6$ and $\phi_0 = 30^\circ$ (port wing down);
3. $M_\infty = 0.85$, $\alpha = 17^\circ$, $Re_{\text{cref}} = 4.9 \cdot 10^6$ and $\phi_0 = 60^\circ$ (port wing down).

3.0 SOLUTION ALGORITHMS

The computational methods used by the partners comprise three multiblock methods and an irregular grid method although all computations were performed using subgrids of a common multiblock grid. The methods solve the Reynolds-averaged Navier-Stokes (RANS) equations for the mean flow, together with some turbulence model equations for the turbulence kinetic energy and eddy viscosity, and an equation of motion for the vehicle moving under the influence of the aerodynamic rolling moment. All the methods apply Jameson's dual time-stepping technique to obtain time-accurate solutions from the underlying steady flow methods.

At Alenia, the computations have been performed using the code UNS3D. It is based on a finite volume, node centred approach operating on an irregular grid. The artificial dissipation model is derived from the non-linear scheme of Jameson. No eigenvalue blending is applied. A five stage Runge-Kutta scheme is used at each real time step. Residual averaging is applied at each Runge-Kutta stage, both to flow and turbulence equations. No multigrid acceleration is employed. The ALE (Arbitrary Lagrangian Eulerian) description is adopted, so that the motion of the fluid is considered in a fixed frame of reference, while the grid is attached to the rotating model. The coupling between the computed rolling moment and the motion of the vehicle is accomplished with a second order scheme, where the vehicle equation of motion is solved at staggered time intervals with respect to the fluid dynamic equations. The two-equations k - R_t wall distance free turbulence model is employed, with Favre averaging to account for compressibility effects, and Menter's SST limiter is implemented. The Wallin-Johansson Explicit Algebraic Stress Model (WJ-EARSM) has been implemented using k - R_t as the basis RANS model.

At NLR, the mean flow equations and the turbulence model are solved as a single system of equations in the flow solver ENSOLV 6.11 that is part of the NLR's CFD system ENFLOW [3]. The spatial discretisation employs a cell-centred finite volume scheme. For the mean flow equations, Jameson-type artificial dissipation fluxes are added consisting of blended first and third order differences with a pressure-based shock sensor. The artificial dissipation terms are implemented with matrix coefficients to enhance the accuracy of the method inside boundary layers. For the turbulence-model equations, artificial diffusive fluxes are also defined using blended first and third order differences, with the scaling factor given by the eigenvalue of the convective flux in the turbulence equations.

For all computations in the present study, a variant of the Wilcox k - ω turbulence model is employed which is better suited to the computation of vortical flows [4] and which resolves the free stream dependency of the solutions [5]. It is well known that the standard model, as with most other two-equation models, over predicts the eddy viscosity within vortex cores which leads to exaggerated diffusion of vorticity [4]. This weakens the vortices and can eliminate secondary separations, especially at low angles of incidence when the vortices are weakest. The enhanced model controls the production of turbulence kinetic energy and hence eddy viscosity through an increase in the production term in the ω equation and has been found to yield significantly improved results for flows of the type which are the subject of this paper. The ratio of the magnitudes of the rate of strain and vorticity tensors is used as the sensor to distinguish between shear layers and vortex cores.

In the steady flow algorithm, the discretised time-dependent system of equations is integrated towards the steady state using a five-stage explicit Runge-Kutta scheme. Local-time stepping, implicit residual averaging, and multi-grid acceleration techniques are applied. The source terms in the turbulence model equations are treated explicitly, and a separate time-step is used to enhance the efficiency of the scheme.

At EADS(M) the calculations were performed using a variant of the FLOWer Code version 116, originally developed in a national German co-operative programme under the direction of DLR, but also with some essential contributions from other participants (Airbus, DASA-M, Technical University of Berlin, etc.) [6]. The code was operated in a Jameson-type mode as a cell-vertex, explicit, multigrid scheme using the finite

volume approach with a five-stage Runge-Kutta scheme for the time integration. The numerical dissipation model is the anisotropic dissipation model as suggested by Jameson, where the dissipation terms are scaled by functions of the convective eigenvalues in each direction of the control volume. Additionally, the dissipative flux vector is optimised by a relaxation between old and new values within the Runge-Kutta scheme.

The variant of the Wilcox $k-\omega$ turbulence model developed at NLR and implemented in the ENSOLV code as described above [4] is also implemented in FLOWer and was used to obtain the results presented here. The governing flow equations and the turbulence transport equations are solved synchronously within the time integration. The solution at each physical time step is obtained rapidly through local time stepping, implicit residual smoothing and the use of a multigrid strategy (3 level W-cycle).

The University of Glasgow used its Parallel Multi-Block 3D RANS solver (PMB3D) for all calculations. The code uses a cell-centred finite volume technique to solve the Euler or RANS equations. The diffusive terms are discretised using a central difference scheme, and the convective terms are discretised using Osher's approximate Riemann solver with MUSCL interpolation. Steady flow calculations proceed in two parts, initially running an explicit scheme, then switching to an implicit scheme to obtain faster convergence. The linear system arising at each implicit step is solved using a Krylov subspace method. The pre-conditioning is based on Block Incomplete Lower-Upper BILU(0) factorisation which is decoupled across blocks. The turbulence model used in the calculations for which results are presented here is again based on the variant of the $k-\omega$ model developed at NLR. At Glasgow, however, the production of turbulence kinetic energy is controlled directly [4] rather than through an increase in ω . The same sensor is used to detect vortex cores. To overcome some convergence difficulties encountered when using this turbulence model, small laminar regions were introduced along the leading edge of the wing and up to 25% of the root chord from the apex. This treatment was used solely to obtain a converged solution.

4.0 OUTLINE DESCRIPTION OF THE EXPERIMENTS

As in the previous study undertaken within Thales JP 12.15 [2], experimental data from DLR formed an essential contribution. The experimental data were obtained partly in the course of the German DLR programme AeroSUM dedicated to manoeuvre flight conditions of a fighter aircraft. Within that programme most of the data were collected at stationary conditions or during forced rolling motions at moderate rolling rates. However, data for a few selected cases were collected at free rolling conditions and a selection of these has been used to help define the test cases for this study and for comparison with computed results.

The tests were performed in the $1\text{ m} \times 1\text{ m}$ transonic wind tunnel DNW-TWG Göttingen at a Mach number of $M=0.85$, Reynolds number 4.9×10^6 based on the chord length c_{ref} and nominal angles of incidence of 9° and 17° . The original intention had been to obtain all the required experimental data using a single wind-tunnel model but this proved not to be satisfactory and some results were obtained using a second model. The AeroSUM model (model 1) was equipped with more than 40 pressure taps and a fast six-component piezo balance in order to take data with a temporal resolution of less than 1 ms. The pressure coefficients C_p for all the individual pressure taps, the force coefficients C_x , C_z , and the rolling moment C_l have been deduced from measured pressure and force values. To ensure correct data evaluation, care was taken to apply the appropriate quantities for mass and moment of inertia experienced by the balance as these were different from those necessary for determining the motion due to the aerodynamic load on the model. In particular, the moment of inertia was strongly influenced by the rotating parts of the complex rolling apparatus. A much more severe problem arose from the effects of mechanical friction of the rolling apparatus. Initial plans to remove the friction by controlling the rolling apparatus could not be realised. As a consequence, tests were required in order to quantify the mechanical friction. Although a considerable effort was expended, no accurate value for the friction could be obtained. The data were

always changing and showed a strong dependence on time and temperature. Also the degree of repeatability was very poor. The final result was a lower and upper limit of the friction of 2 Nm and 4 Nm, respectively.

As the quality of the results at the desired flow conditions for comparison with the computed solutions was not very satisfactory, it was decided to perform an additional test in the course of flow field measurements applying PIV. Another model, model 2, slightly different from model 1 and less instrumented had to be used. Only 1 instead of more than 40 pressure taps was available. The balance was replaced by a dummy. In order to get the same dynamic behaviour mass had to be added to the model. The final mass and moment of inertia of model 2 were sufficiently close for the differences in dynamic behaviour to be ignored.

5.0 EQUATION OF MOTION OF THE VEHICLE

5.1 One Degree of Freedom Motion in Roll

The Reynolds-averaged Navier-Stokes equations in the computational methods of the participants were augmented by the simple equation of motion describing freedom of the vehicle to roll about its fuselage axis. The equation governing the motion is therefore

$$I_{\phi} \phi_{tt} = L(\phi, \phi_t)$$

where I_{ϕ} is the moment of inertia of the model about the fuselage axis, ϕ is the roll angle, L is the couple producing the motion and t is time. In the present work, L represents the aerodynamic moment and damping, and the effect of mechanical friction in the bearing of the sting support mechanism. A dimensionless form of the equation suitable for augmenting the RANS equations in a computational method is provided by the scaling

$$I_{\phi} = m r_{\phi}^2 = m R_{\phi}^2 c_{ref}^2,$$

$$L(\phi, \phi_t) = \frac{\rho_{\infty} u_{\infty}^2}{2} S (C_l(\phi, \phi_t) - \bar{C}_{lf}(\phi, \phi_t)) l_r,$$

$$\mu = \frac{2m}{\rho_{\infty} S l_r}$$

and

$$\tau = \frac{t}{t_{ref}}.$$

The mass of the model is m , r_{ϕ} is the radius of inertia and R_{ϕ} is the radius of inertia scaled by the reference chord, c_{ref} ; S is a wing reference area, l_r is the moment arm used to define the rolling moment and μ is a mass ratio. The free stream speed and density of the air are u_{∞} and ρ_{∞} respectively. τ is the computational time and t_{ref} is a reference time that depends on the non-dimensionalisation used in the flow prediction code. C_l is the aerodynamic rolling moment coefficient while \bar{C}_{lf} is the roll moment damping coefficient due to mechanical friction. The latter is written in a general form as a function of the roll angle and roll rate and is positive since it always acts so as to oppose the vehicle motion. The equation of motion may therefore be written in non-dimensional form as

$$\phi_{\tau\tau} = \frac{u_{\infty}^2 t_{ref}^2}{\mu R_{\phi}^2 c_{ref}^2} (C_l(\phi, \phi_{\tau}) - \bar{C}_{lf}(\phi, \phi_{\tau})).$$

5.2 Mathematical Model of Mechanical Friction in the Wind-Tunnel Support Rig

In free flight, \overline{C}_{lf} is, of course, zero. In the wind tunnel, however, it is non-zero but its form and magnitude proved impossible to determine with confidence, as discussed in Section 4.0, above. A study was therefore undertaken at EADS(M) in which a series of calculations was performed using different models for the mechanical friction and the results were compared with experimental data in order to obtain a mathematical model which reproduced the experimental data most closely. It was assumed that \overline{C}_{lf} was of the form $C_{lf}\phi_\tau + C_{lf}sign(\phi_\tau)$. The term $C_{lf}\phi_\tau$ describes linear friction, depending linearly on the rotation speed, and the term $C_{lf}sign(\phi_\tau)$ describes the constant, Coulomb type of mechanical friction. The linear friction can be treated numerically very easily, and thus this form is widely used. Preliminary Euler calculations have however shown that the type of motion observed in the experiment could be reproduced only with the constant, Coulomb type of mechanical friction, as can be seen in Figure 3. Other types of motion, with final stable positions at non-zero roll angles, can also be reproduced as will be seen in Section 6.0, Figures 11 and 14.

A linear friction law results only in a damping of the amplitude; the motion will always end at a trim position since the mechanical friction is zero when the angular velocity is zero and a non-zero aerodynamic rolling moment would cause the vehicle to move. In contrast, it should be noted that with a constant friction law, there is a possibility that ϕ_τ will become zero while $|C_l(\phi, \phi_\tau)|$ is less than C_{lf} . The friction model has been implemented in all of the computational methods so that, should this circumstance arise at any stage during the motion, ϕ_τ will remain zero, i.e. the motion will cease when the vehicle is not exactly in trim. It is unlikely that ϕ_τ will become exactly zero at any time step of the calculation, of course, and so if the angular velocity changes sign between time steps, interpolation is used to find the aerodynamic moment at the time ϕ_τ becomes zero and the vehicle motion is continued at the next time step only if the magnitude of the aerodynamic moment is greater than the static friction moment. Calculations using different values of C_{lf} were performed at EADS(M) for each of the test cases and comparison with experimental data was used to determine the value that gave the best overall agreement. This value was then used by all participants for calculations in which an allowance was made for friction in the tunnel support rig.

The predicted behaviour of the vehicle and the method of integrating the mathematical model in time are affected by the detailed implementation of the model. Two approaches are in common use, the first in

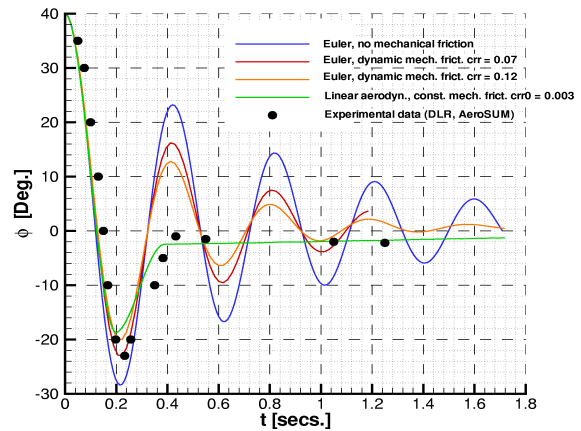


Figure 3: Effect of mechanical friction. Case 1: $M_\infty=0.85$, $\alpha=9^\circ$, $\phi_0=40^\circ$. Euler with 1 DOF coupling.

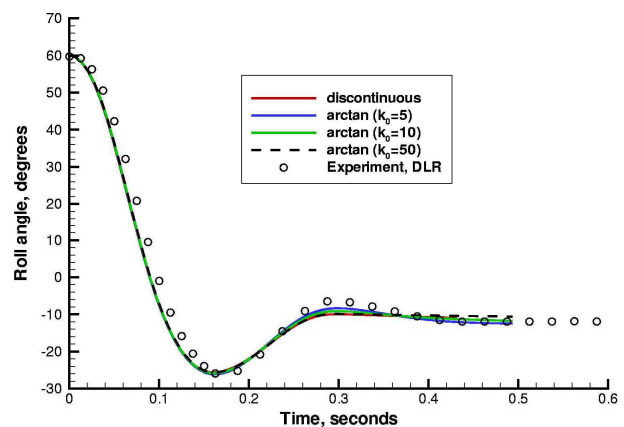


Figure 4: The response of the roll angle for both discontinuous and continuous (various values of k_0) frictional models for case 3.

which the discontinuity is modelled directly and a second in which the frictional moment is a continuous function, rapidly varying in the neighbourhood of $\phi_\tau = 0$. The two approaches were investigated at NLR in the context of the test cases of the present study. The mechanical friction was approximated by the function $\frac{2}{\pi} \arctan\left(k_0 \frac{d\phi}{d\tau}\right)$ for the second approach. The degree of approximation to the discontinuous model can be controlled using the parameter k_0 that represents the gradient of the friction moment at zero velocity. The greater the value of k_0 the better the approximation but the more stiff the differential equation. Some of the results are summarised in Figure 4 which shows the predicted vehicle motion (roll angle versus time) for the third test case for the discontinuous model and the continuous model with three values of k_0 . In fact, the effects of varying k_0 become significant only towards the end of the motion when the velocity is small. A value of $k_0 = 50$ yields results that are comparable to those obtained using the discontinuous model but the equation is unhelpfully stiff. Participants were therefore allowed to choose which approach to adopt in their own methods. The results from NLR were obtained using the continuous model with a value of $k_0 = 10$. The Newton iteration method was used to solve the equation.

6.0 RESULTS AND DISCUSSION

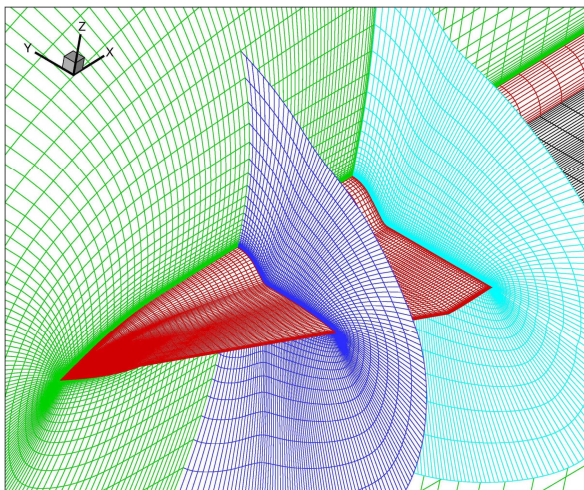


Figure 5: General view of the computational grid

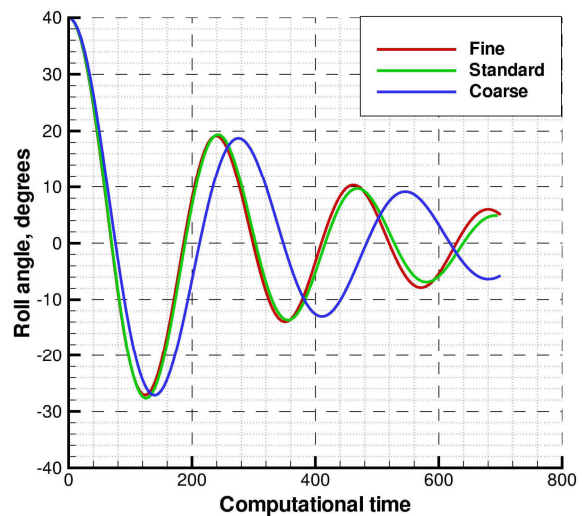


Figure 6: The effect of grid fineness on predicted vehicle motion. Case 1: $M_\infty=0.85$, $\alpha=9^\circ$, $\phi_0=40^\circ$.

The computational grid was generated at EADS(M) and is of C-O topology. On the wing surface the grid is conical so that all members of one family of grid lines pass through the apex of the wing while each member of the second family is at a constant value of the streamwise co-ordinate. There is therefore a singular line from the apex to the upstream far-field boundary and an O-type singularity from the wing tip trailing edge to the downstream far-field boundary on each side. Note that the full configuration is modelled to enable asymmetric flows to be calculated. In the standard grid, there are 144 intervals in the streamwise direction from the apex, 320 in the circumferential direction around the wing and 64 in the normal direction from the wing surface to the far-field boundary, giving 2,949,120 cells in total. The grid was designed to provide sufficient resolution of the viscous layers and to suit the vortical flows associated with delta wings. A general view of the grid is presented in Figure 5. To check the adequacy of the grid, a coarser version was derived by omitting alternate points in each co-ordinate direction and a finer version was generated having twice the number of intervals in the spanwise and normal-to-surface directions; it therefore contained just under 12 million cells. Figure 6 shows the vehicle motion for case 1 predicted by

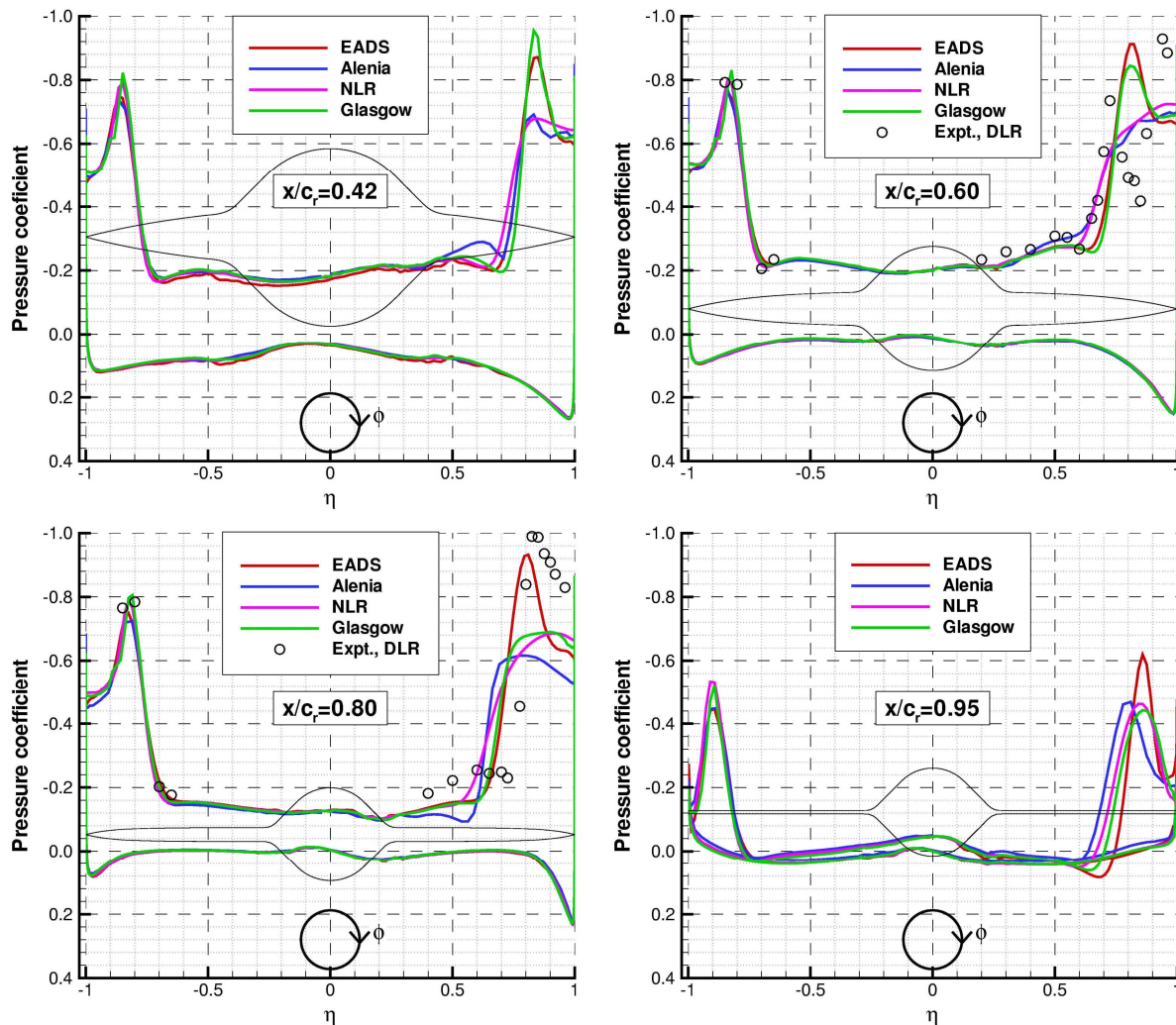


Figure 7: Spanwise distributions of surface pressure coefficient. Case 1: $M_\infty=0.85$, $\alpha=9^\circ$, $Re=4.9 \cdot 10^6$, $\phi_0=40^\circ$.

Glasgow using each of the grids. The fine grid calculation was performed using a cluster of 40 processors (2.5 GHz) and took approximately one day for the initial steady flow calculation together with a further day for the free-to-roll calculation. It is clear that the PMB3D code produces approximately the same result using the standard and fine grids, but that the coarse grid is inadequate in this case. The corresponding initial surface pressure distributions (not shown) yield the same conclusion which is to be expected since they drive the initial motion. The standard grid was therefore used by Glasgow, NLR and EADS(M) to obtain their results for the three test cases. Alenia used a coarse grid, obtained from the standard grid by omitting alternate points in both the streamwise and circumferential directions, because of limitations on its available computing resources.

The initial distributions of surface pressure coefficient predicted by all participants are shown for case 1 in Figure 7. The figure is viewed as if from ahead of the aircraft so that the port wing is on the right, $\eta > 0$. The local cross-section shape of the configuration is superimposed on each plot and the circle with arrow at the bottom centre shows the direction of increasing ϕ . At an angle of incidence of 9° and an initial roll angle of 40° , the effective angle of incidence is small and there is significant sideslip which reduces the effective sweep of the port wing. At these conditions, the computed flows are attached in the neighbourhood of the apex. The flow predicted by NLR remains attached over most of the port wing and the prediction from Alenia is similar, although there are signs of vortical flow development at $x/c_r=0.42$ in

the latter which are not sustained downstream. In the predictions from EADS(M) and Glasgow, however, the flow separates along a line with origin on the port wing upper surface and extending aft and outboard to the leading edge at a point forward of $x/c_r=0.42$. The separation line then continues along the leading edge so that well defined vortices develop above the port wing. Vortical flow develops above the starboard wing in all solutions, as expected. Only in the solution from EADS(M) is the suction maintained over the rear part of the port wing. In several of the solutions, it is possible to see the signs of an additional suction peak outboard of the primary peak, at approximately 97% semispan. This indicates a secondary separation induced by the adverse pressure gradient under the primary vortex. Experimental data available for the $x/c_r=0.6$ and $x/c_r=0.8$ stations are also shown in the figure. At $x/c_r=0.8$, there is fair agreement with the solution from EADS(M) though the primary suction is a little stronger and the suction peak is slightly more outboard in the experiment. However, at $x/c_r=0.6$ the experimental pressure distribution is clearly of a different character. There are two high suction peaks at about 72% and 94% semispan. This indicates that the separation line on the forward part of the wing reaches the leading edge at between $x/c_r=0.6$ and $x/c_r=0.8$ in the experiment and that, at $x/c_r=0.6$, the flow remains attached around the leading edge to about 85% semispan; it then separates before reattaching at 60% semispan. Such a flow topology would yield the conventional leading edge suction peak of attached flow outboard, and a second suction peak inboard induced by the vortex that develops from the separation. It is possible for viscous flow to remain attached around a corner and it is known that the leading edge of the model is not as sharp as that of model 2 (see Section 4.0). There is a further small suction peak at about 50% - 60% semispan over much of the wing in both computed and experimental flows. This may be an effect of the high relative thickness of the fuselage in the forward part of the configuration, but recent work of Hummel [7] suggests an alternative explanation. In a case studied by Hummel, laminar separation occurs along the separation line on the upper surface of the wing. The separated flow gives rise to a weak vortex producing a small suction peak at 60% - 70% semispan in that particular case. Aft of the point at which the separation line meets the leading edge, high vorticity is shed into a strong vortex, with associated strong suction peak outboard and the original, weak vortex continuing as a second branch (i.e. of the same sign) with associated weak suction peak inboard. In the present experiment, the status of the boundary layers ahead of separation is not known. However, for the predictions from EADS(M), NLR and Alenia, fully turbulent flow over the wing is specified, whereas for the prediction from Glasgow, laminar flow is specified ahead of the 25% centreline chord location, yet the predicted flows do not divide into these groups. It may be therefore that a bubble-type vortex forms from the initial separation as described by Hummel, giving rise to this small, inner suction peak, while the primary vortex is as described above for the predictions from Glasgow and EADS(M) and is double branched. Further analysis of the computed flows or flow visualisation in future wind-tunnel tests should confirm the true topology of the flow.

The model is released from rest at its initial roll angle of 40° . All partners calculated the subsequent motion without allowing for the mechanical friction in the wind tunnel model support sting. The results are shown in Figure 8 in which the predicted roll angle is plotted against computational time. The vehicle undergoes damped oscillations about $\phi=0$, at which it will eventually come to rest. Comparison with Figure 6 indicates that the lower frequency of oscillation predicted by Alenia results from the use of the coarse grid. There is good agreement in the predicted frequency from the other solutions. The compact vortex in the solution from EADS(M), with high peak suctions extending further aft over the port wing than in the other predictions, produces a higher initial rolling moment and lower aerodynamic damping, and consequently a higher amplitude of oscillation. The variation of rolling moment with computational time is shown in Figure 9.

The angle of incidence was increased to 17° for case 2, while the initial roll angle at which the model was released was 30° . Figure 10 shows the initial surface pressure distribution computed by each of the partners. The agreement is generally good with EADS(M) and Glasgow again predicting more compact vortices than NLR or Alenia, and Glasgow predicting the highest peak suction on the forward port wing. All solutions show the effect of a well developed primary vortex above the starboard wing and a clear secondary separation. The strong vortex above the port wing breaks down between 60% and 80% chord,

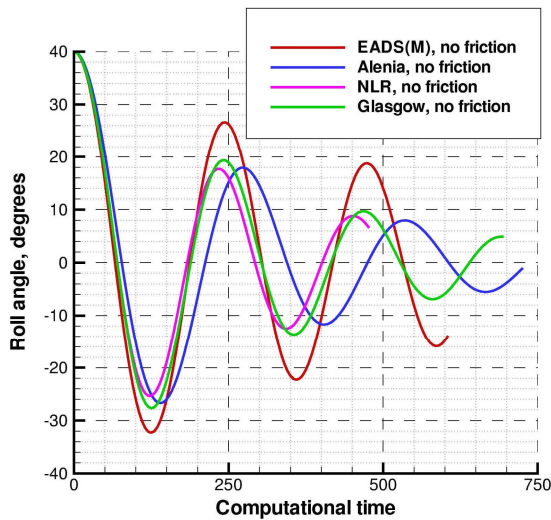


Figure 8: Variation of roll angle with computational time. Case 1: $M_\infty=0.85$, $\alpha=9^\circ$, $Re=4.9 \cdot 10^6$, $\phi_0=40^\circ$.

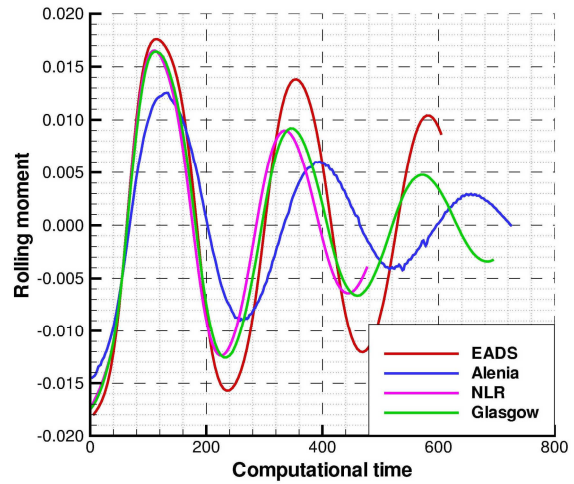


Figure 9: Variation of rolling moment with computational time. Case 1: $M_\infty=0.85$, $\alpha=9^\circ$, $Re=4.9 \cdot 10^6$, $\phi_0=40^\circ$.

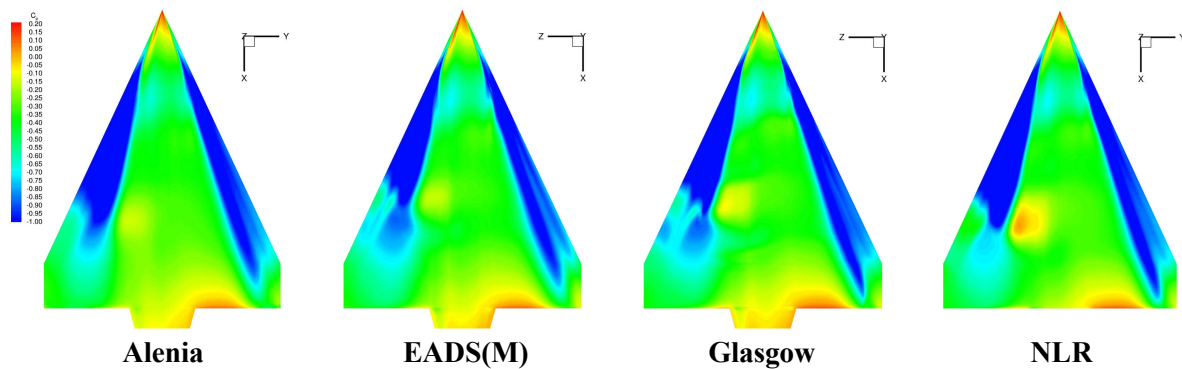


Figure 10: Computed surface pressure distributions. Case 2: $M_\infty=0.85$, $\alpha=17^\circ$, $Re=4.9 \cdot 10^6$, $\phi_0=30^\circ$.

but there is clear evidence of a secondary separation from the forward part of the wing. The region of high pressure inboard of the vortex footprint at 60% - 70% chord is associated with the vortex burst.

The significantly higher suctions than predicted for case 1, together with the high degree of asymmetry in the flow, lead to much higher initial rolling moments in this case. In order to aid comparison with the vehicle motion observed in the wind tunnel, the mechanical friction in the model support sting was incorporated in the computations as described above. The predicted motions and associated rolling moments are shown in Figures. 11 and 12. The agreement between experiment and the prediction from EADS(M) is good, as expected, since comparison of predictions from EADS(M) with experiment was the basis for determining the computational model of mechanical friction used by all partners. The model rolls towards the symmetric position attained in Case 1 ($\phi=0$) but halts before reaching it and rolls back towards the starting point. However, it again comes to rest without significant overshoot at about $\phi=12^\circ$ and remains there. The final roll angle predicted by EADS(M) is slightly lower, but this may simply be the result of the friction in the support sting. The results from NLR and Glasgow are similar to each other but differ significantly from that from EADS(M); they show the model finally coming to rest in the symmetric attitude. Although the initial rolling moments predicted by EADS(M) and Glasgow are very close, the motion predicted by EADS(M) is less damped and the angular velocity attained by the vehicle

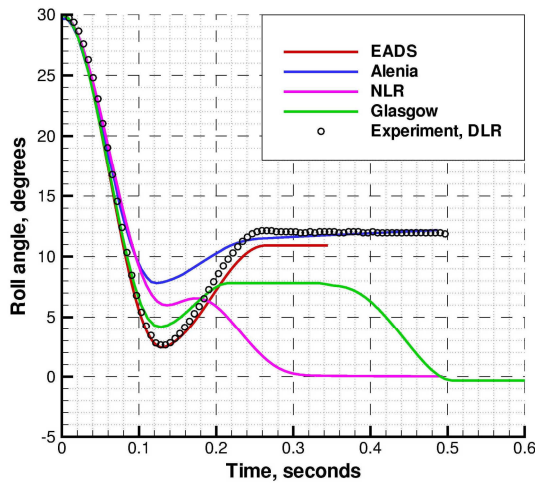


Figure 11: Variation of roll angle with time. Case 2: $M_\infty=0.85$, $\alpha=17^\circ$, $Re=4.9 \cdot 10^6$, $\phi_0=30^\circ$.

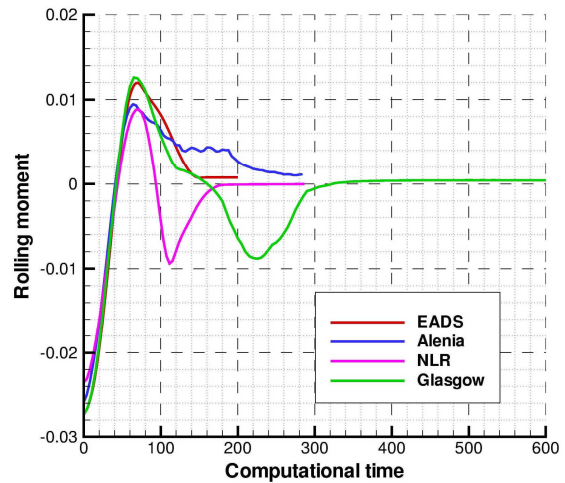


Figure 12: Variation of rolling moment with computational time. Case 2: $M_\infty=0.85$, $\alpha=17^\circ$, $Re=4.9 \cdot 10^6$, $\phi_0=30^\circ$.

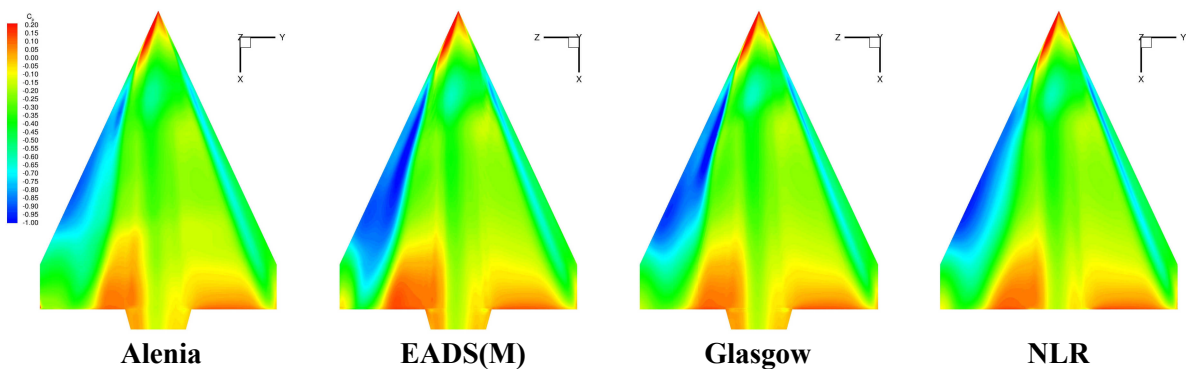


Figure 13: Computed surface pressure distributions. Case 3: $M_\infty=0.85$, $\alpha=17^\circ$, $Re=4.9 \cdot 10^6$, $\phi_0=60^\circ$.

on its return is significantly higher than predicted by Glasgow. In the final position of the vehicle in the experiment and the prediction from EADS(M), there is a burst vortex above the port wing and a weaker vortex above the starboard wing which exactly balance each other and lead to zero rolling moment at the non-zero roll angle. In the Glasgow prediction, the vehicle comes to rest at a roll angle of approximately 8° and remains there for some time; the predicted aerodynamic rolling moment is less than the static friction in the support sting. However, the unsteady flow continues to develop, the rolling moment increases and eventually the vehicle again begins to move, in this case back towards $\phi=0$. In the final position, there is vortex breakdown above both wings. The prediction from NLR is similar but without the long pause in the motion. Additional experimental data reveal that the case is close to a change in character of the motion of the model in the wind tunnel. At slightly higher initial roll angles, the tunnel model will also come to rest in the symmetric position $\phi=0$. The final roll angle predicted by Alenia is approximately 10° . This apparently good agreement with experiment and the prediction from EADS(M) may be simply a consequence of the use of the coarse grid by Alenia, however, since the peak magnitude of the angular velocity was lower than in any other prediction and the roll angle fell to only 8° before the vehicle reached its final trim position.

The boundary conditions for case 3 were the same as those for case 2 but the initial roll angle was increased to 60° . The initial distributions of surface pressure are shown in Figure 13. The effective angle

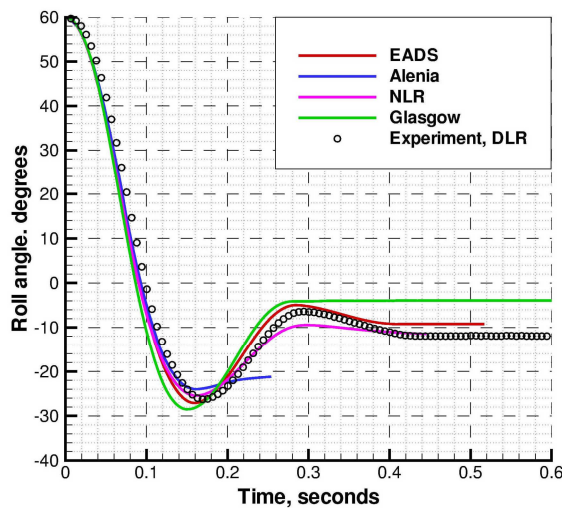


Figure 14: Variation of roll angle with time. Case 3: $M_\infty=0.85$, $\alpha=17^\circ$, $Re=4.9 \cdot 10^6$, $\phi_0=60^\circ$.

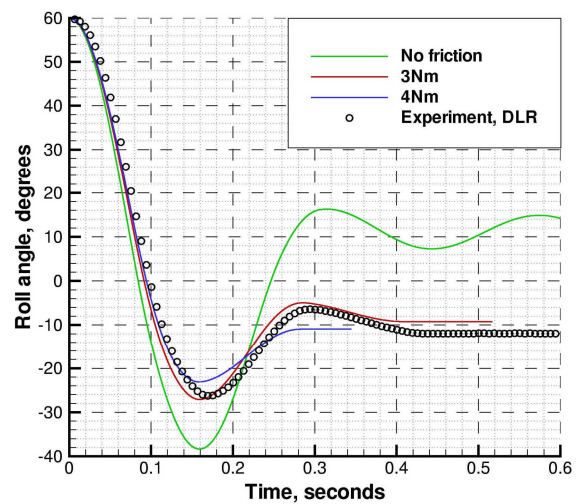


Figure 15: Variation of roll angle with time. Predictions from EADS(M) for different coefficients of mechanical friction. Case 3: $M_\infty=0.85$, $\alpha=17^\circ$, $Re=4.9 \cdot 10^6$, $\phi_0=60^\circ$.

of incidence at the start of the motion is quite small and, in consequence, the vortex over the starboard wing is very weak. The flow over the port wing is rather more complex. The predictions from EADS(M) and Glasgow suggest vortical flow development from the forward part of the wing and a significant secondary flow over the rear. NLR and Alenia predict generally lower suction over the forward part of the wing with more extensive secondary flow development. Spanwise cuts of the pressure distributions suggest that the flow is attached at the leading edge over much of the wing in the predictions from NLR and Alenia. Further investigation is required to confirm the topology of the flow in all cases.

The predicted vehicle motion is shown in Figure 14. There is good agreement between experiment and the predictions from EADS(M) and NLR. As in case 2, it should be noted that comparison between EADS(M) predictions and the experimental data were used to determine and define the mathematical model of the mechanical friction and so the good agreement in this case is expected. Glasgow predicts a more rapid initial acceleration and higher amplitude of oscillation so that the vehicle returns almost to the symmetric attitude at the end of the first cycle, where it is caught by the effect of mechanical friction. The time step length used by Glasgow was reduced from $\Delta\tau=5$ to $\Delta\tau=2$ and again to $\Delta\tau=1$ but this had no significant effect on the final solution. Although the vehicle has undoubtedly come to rest in the solution from Alenia, and the predicted rolling moment is approximately equal to that from Glasgow (being less than or equal to the static friction), the result is inconclusive. It may again be the simple consequence of using the coarse grid but further investigation is required. Figure 15 shows the vehicle motion predicted by EADS(M) for two values of the coefficient of mechanical friction in the model, and with no allowance for mechanical friction. This, together with similar results for cases 1 and 2, and the results shown in Figure 3, were used to define the model of the mechanical friction and determine an appropriate coefficient. A coefficient equivalent to 3 Nm was used by all participants to compute the results for test cases 2 and 3. Figure 15 is particularly interesting because it shows that singular behaviour is not a feature only of wind-tunnel models with the associated mechanical friction in the support sting. The result when the effects of mechanical friction are not included, representative of free flight, shows that, after the first cycle, the vehicle undergoes damped oscillations about the final trim position of case 2 ($\phi \approx 11^\circ$). Thus CFD offers the capability for simulating both wind-tunnel and free flight experiments and hence reconciling differences observed in results from the two types of experimental technique.

At the end of the motion observed in the experiment and predicted by EADS(M) and NLR, there is a well

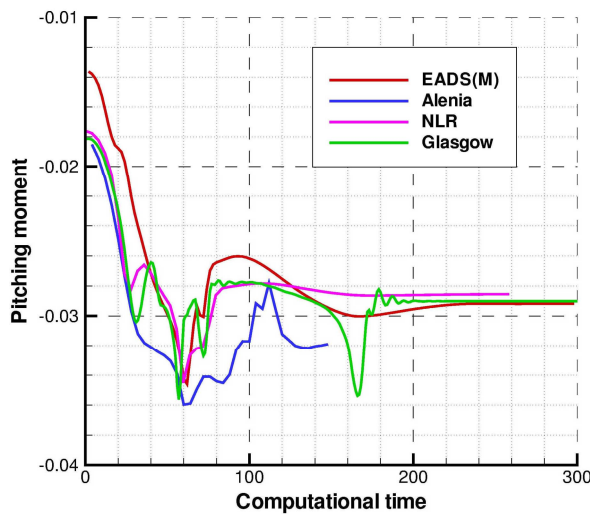


Figure 16: Variation of pitching moment with computational time. Case 3: $M_\infty=0.85$, $\alpha=17^\circ$, $Re=4.9 \cdot 10^6$, $\phi_0=60^\circ$.

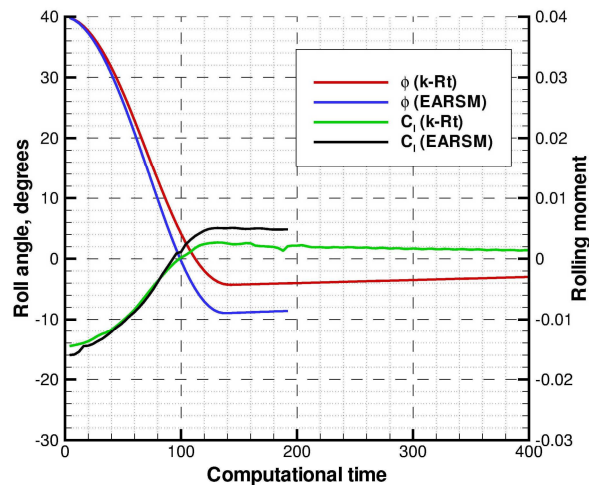


Figure 17: Variation of roll angle and rolling moment with computational time for two different turbulence models. Case 1: $M_\infty=0.85$, $\alpha=9^\circ$, $Re=4.9 \cdot 10^6$, $\phi_0=40^\circ$, with mechanical friction.

developed vortex above the port wing but the vortex above the starboard wing has broken down. This is therefore the mirror image of the flow observed in the experiment or predicted by EADS(M) for case 2. In the flow at the end of the motion predicted by Glasgow, vortex breakdown has occurred above both wings. These differences in predicted flow regimes have a significant impact on the forces and moments on the vehicle. For example, the drag coefficients predicted by EADS(M) and Glasgow at the end of the motion are respectively 0.0392 and 0.0707. The predicted variation of pitching moment with computational time is shown in Figure 16 for all contributors. Although the test case is not representative of real flight, the figure illustrates the complex behaviour of forces and moments that can arise. Computational methods can help identify, explore and understand such behaviour and this is the first step in avoiding, controlling or exploiting it.

Finally, it is clear from the results presented so far that it is not yet possible to predict accurately, with confidence, complex unsteady viscous flows. In particular, prediction of separation location and the onset and location of vortex breakdown present considerable challenges. It is to be expected that the turbulence model employed will influence the prediction of the flow, especially these features of the flow, and hence also the consequent vehicle motion. To help quantify this influence, a series of calculations was performed at Alenia using both the $k-R_t$ model and the $k-R_t$ model with explicit algebraic Reynolds stress modelling as described in Section 3.0. A typical result is shown in Figure 17. The flow conditions are those of case 1 but, on this occasion, an allowance has been made for mechanical friction (3 Nm) in the model support rig. The variation of roll angle and rolling moment with computational time is presented for each of the turbulence models. The final flow characteristics are the same in each case. However, the effect of applying the EARSM is that, in general, a more compact vortex is predicted, compared to that obtained from the use of the $k-R_t$ model alone, and where vortex breakdown occurs, the location of the breakdown is further forward. In the particular situation of case 1, it appears that the flow predicted using the $k-R_t$ model alone is attached over most of the port wing at the start of the motion. In contrast, the flow predicted using the EARSM clearly separates at the leading edge along most of its length. Thus there are significant differences in initial rolling moment that produce differences in model acceleration and hence a divergence in predicted roll angles. This, in turn, leads to increased differences in predicted rolling moment. It seems likely that there will be other cases in which a change of turbulence model will have a greater impact on the prediction. It is clear, therefore, that turbulence modelling remains an important factor in the exploitation of CFD and, as always, care should be exercised in the choice of turbulence

model for the particular application. The importance of the turbulence model has recently been confirmed by Hummel [7] who has taken the matter further by showing that the state of the boundary layers on the wing surface will have a significant influence on the location of separation and subsequent vortex development, and on the surface pressure distribution. It is therefore important not only to be able to predict accurately the development of turbulent shear layers, but also the development of laminar boundary layers and the location of the onset of transition. The latter will be increasingly important for lower Reynolds numbers but may still be significant at the Reynolds numbers of the present test cases.

7.0 CONCLUSIONS

The work presented in this paper concerns an extensive collaborative exercise which sought to demonstrate the feasibility of simulating air vehicle manoeuvre in complex flow regimes and validating the capability that was developed. The objective was achieved successfully through a series of carefully performed experiments combined with a comprehensive computational investigation. The results show that a robust capability has been developed and open the way for the calculation of complete six-degrees-of-freedom manoeuvre. The results further show that singular behaviour is not a feature only of models in wind tunnels and so the capability will enable differences between wind tunnel and free flight results to be reconciled. The simulation of a manoeuvring air vehicle, including the response to varying control settings, is an important goal for the exploitation of computational fluid dynamics. Typical computing times currently of the order of one day on a cluster of p.c.s mean that such applications will soon become routine.

Many operational air vehicles operate at high speeds, high angles of incidence and high manoeuvre rates. At such conditions, non-linear behaviour must be expected. A capability for assessing configurations and exploring limited regions of the flight envelope will therefore enable risks to be reduced. Some future air vehicles will also experience non-linear behaviour at certain conditions and an ability to identify this early in the design process will reduce costs or the need to restrict the flight envelope later in the procurement. The work presented here represents a step in the development and demonstration of the required capability. It is a precursor step that will eventually provide one more tool for the calculation of the dynamic stability derivatives needed for the assessment of vehicle stability. Furthermore, it is a step towards meeting the strategic objective of a capability for simulating manoeuvre, taking into account aerodynamics, flight mechanics, control deployment, aeroelasticity and engine power settings.

8.0 ACKNOWLEDGEMENTS

The authors would like to thank Prof. D. Hummel (Technical University, Braunschweig) and Dr. K.J. Badcock for many valuable discussions.

9.0 REFERENCES

- [1] Fritz, W., Arthur, M.T., Brandsma, F.J., Bütetfisch, K.-A. and Ceresola, N., "Time Accurate Euler Calculations of Vortical Flow over a Delta Wing in Rolling Motion", RTO/AVT Vortex Flow Symposium, Loen, Norway, 2001.
- [2] Soemarwoto, B.I., Boelens, O.J., Fritz, W., Allan, M., Arthur, M.T., Ceresola, N. and Bütetfisch, K., "Towards the Simulation of Unsteady Maneuver Dominated by Vortical Flow", AIAA Applied Aerodynamics Conference, Paper 2003-3528, Orlando, June, 2003.
- [3] Boerstoeel, J.W., Kassies, A., Kok, J.C. and Spekreijse, S.P., "ENFLOW, A full-functionality system of CFD codes for industrial Euler/Navier-Stokes flow computations", NLR TP-96286 (presented at

the 2nd International Symposium on Aeronautical Science and Technology, Jakarta, 1996), 1996.

- [4] Brandsma, F.J., Kok, J.C., Dol, H.S. and Elsenaar, A., Leading edge vortex flow computations and comparison with DNW-HST wind tunnel data, in *Proceedings of the RTO/AVT Vortex Flow Symposium, Loen, Norway, 2001*, RTO-MP-069(I), ISBN 92-837-0022-8.
- [5] Kok, J.C., “Resolving the dependence on freestream values for the k- ω turbulence model”, *AIAA Journal*, Vol. 38, No. 7, 2000, pp. 1292-1294.
- [6] Kroll, N., Aumann, P., Bartelheimer, W., Bleecke, H., Eisfeld, B., Lieser, J., Heinrich, R., Kuntz, M., Monsen, E., Raddatz, J., Reisch, U. and Roll, B., “FLOWer Installation and User Handbook”, DLR Doc. Nr. MEGAFLOW-1001, 1998.
- [7] Hummel, D., Effects of boundary layer formation on the vortical flow above slender delta wings, presented at the RTO AVT Specialists’ Meeting on “Enhancement of NATO Military Vehicle Performance by Management of Interacting Boundary Layer Transition and Separation”, Prague, October 2004, and published in RTO-MP-AVT-111.

10.0 NOMENCLATURE

C_D	drag coefficient
C_L	lift coefficient
C_l	rolling moment coefficient
$\overline{C_{lf}}(\phi, \phi_\tau)$	general functional form of the coefficient of mechanical friction
C_{lf}	(magnitude of) coefficient of mechanical friction
C_m	pitching moment coefficient
C_p	pressure coefficient
c_r	centre line chord length
c_{ref}	reference chord length, equal to the wing centre line chord length
M_∞	free-stream Mach number
Re_{cref}	Reynolds number based on the reference chord length c_{ref}
x, y, z	Cartesian co-ordinates of the body axis system
t	time
α	angle of incidence
τ	computational time
ϕ	roll angle
ϕ_0	initial roll angle